Universal mask for hard X rays

DAVID CEDDIA,[1] ALALEH AMINZADEH,[2] PHILIP K. COOK,[3] DANIELE PELLICCIA,[4] ANDREW M. KINGSTON,[2,5] AND DAVID M. PAGANIN[1,*]

[1] *School of Physics and Astronomy, Monash University, Victoria 3800, Australia*
[2] *Department of Materials Physics, Research School of Physics, The Australian National University, Canberra ACT 2601, Australia*
[3] *ESRF, The European Synchrotron, 71 Avenue des Martyrs, CS 40220, 38043 Grenoble Cedex 9, France*
[4] *Instruments and Data Tools Pty Ltd, PO Box 2114, Rowville VIC 3178, Australia*
[5] *CTLab: National Laboratory for Micro Computed-Tomography, Advanced Imaging Precinct, The Australian National University, Canberra, ACT 2601, Australia*
[*] *Corresponding author: david.paganin@monash.edu*

Abstract: Multiple exposures, of a single illuminated non-configurable mask that is transversely displaced to a number of specified positions, can be used to create any desired distribution of radiant exposure. An experimental proof-of-concept is given for this idea, employing hard X rays. The method is termed "ghost projection", since it may be viewed as a reversed form of classical ghost imaging. The written pattern is arbitrary, up to a tunable constant offset, together with a limiting spatial resolution that is governed by the finest features present in the illuminated mask. The method, which is immune to both proximity-correction and aspect-ratio issues, can be used to make a universal lithographic mask in the hard-X-ray regime. Ghost projection may also be used as a dynamically-configurable beam-shaping element, namely the hard-X-ray equivalent of a spatial light modulator. The idea may be applied to other forms of radiation and matter waves, such as gamma rays, neutrons, electrons, muons, and atomic beams.

1. Introduction

The concepts established in Refs. [1–3] show that building signals out of noise, *e.g.* building images out of random maps, is not as contradictory as it might sound. Here we experimentally demonstrate the writing of arbitrary distributions of radiant exposure, using a single illuminated transversely-displaced non-configurable patterned mask. Stated differently, we establish proof-of-concept for a universal hard-X-ray mask. The underpinning principle is very general, and can be applied to a variety of radiation and matter-wave fields—*e.g.* neutrons [4], electrons [5], muons [6, 7], atomic beams [8], ion beams [9], and gamma rays—for which configurable beam-shaping elements either do not exist, or have low spatial resolution. Three future applications drive this work: (i) an X-ray spatial light modulator or data projector; (ii) a universal hard-X-ray photolithographic mask; (iii) 3D short-wavelength high-resolution printing in volumetric additive manufacturing [10–13], as well as for sculpting desired 3D distributions of X-ray dose, *e.g.* for intensity-modulated radiotherapy [14].[1]

The method, termed "ghost projection" (GP) [2,3], is a reversed form of classical computational ghost imaging [15]. Ghost imaging (GI) is an indirect imaging technique, originally developed in the context of entangled-photon quantum optics, but later shown to have a classical variant which is of primary concern here [16–18]. GI requires the splitting of a patterned illumination (or speckled beam). One part interacts with the sample, reducing the total intensity transmitted, which is recorded by a bucket (single-pixel) detector. The second part does not interact with the sample, but rather is measured directly by a pixel array detector, forming the reference image. An image of the sample is never recorded directly. Rather, the image is reconstructed by correlating bucket signal and reference image. For classical illumination the bucket measurements may be viewed as decomposition coefficients in a non-orthogonal-function expansion of the unknown

[1] These potential applications are examined in more detail in the Discussion (Section 4).

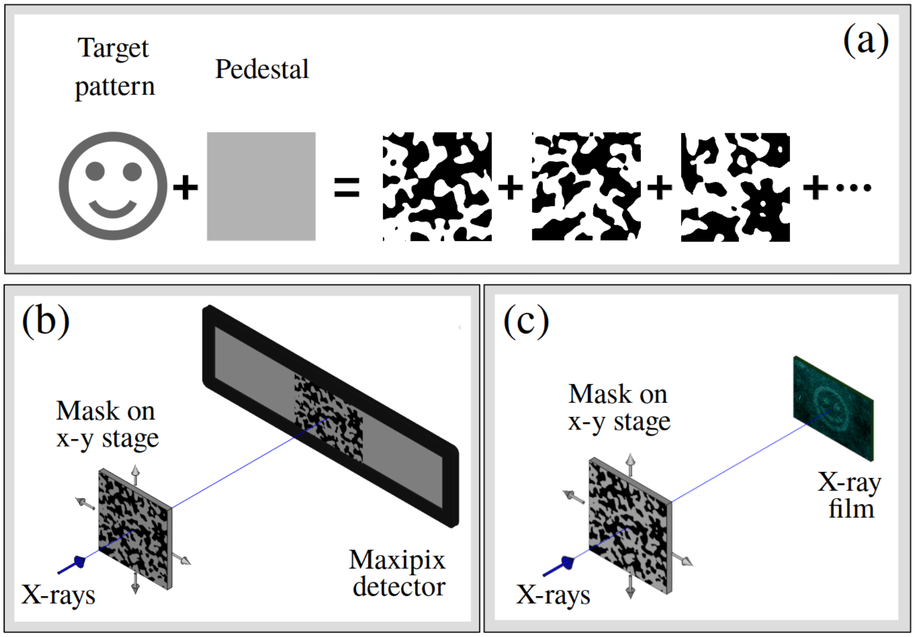

Fig. 1. (a) Building signals out of noise. Any 2D target pattern can be expressed as a linear combination of speckle maps, up to an additive offset ("pedestal"). Experimental "ghost projection", using an illuminated random mask and (b) digital pixel-camera (Maxipix) detection or (c) film-based detection.

sample [19–21] (cf. Refs. [22, 23]). Such an expansion is sketched in Fig. 1(a). Classical GI measures intensity correlations (bucket signals) between an unknown object and a set of patterned illuminations, in order to reconstruct an unknown object. In contrast, ghost projection—namely the method employed in the present work—seeks to *establish such correlations in order to create a desired image (spatial distribution of radiant exposure)*. The fundamentals of GP are developed in Refs. [1, 2] and an understanding of the practical considerations are explored in Ref. [3]. Supplement 1 Section 1 provides an abstract description of GP that is based on the linear algebra of high-dimensional vector spaces, with Supplement 1 Section 2 providing a more detailed discussion comparing and contrasting ghost imaging and ghost projection.

A generic ghost-projection experiment is sketched in Figs. 1(b) and 1(c). Here, a source illuminates a spatially-random[2] non-configurable mask, thereby generating a speckle pattern over a specified illumination plane. The pattern that is produced by the mask, over the illumination plane at a distance Δ downstream of the mask, is assumed to be known.[3] If Δ is sufficiently large and the mask is thin, this distance between the mask and the illumination plane generates speckle via Fresnel diffraction, which may also be spoken of as propagation-based phase contrast [24] or out-of-focus contrast [5]. If Δ is sufficiently small and the mask is thin, structured illumination will instead be based on mask absorption. Thick random masks may also be employed to generate speckles [25, 26] for the purposes of ghost projection. Regardless of the speckle-generation scenarios, by transversely scanning the mask to specified locations, any pattern of time-integrated radiant exposure can be imprinted on the illumination plane, up to both (i) an additive constant (termed a "pedestal," see Fig. 1(a)) and (ii) a limiting spatial resolution equal to the finest length

[2]While most of the masks we employ in our experiment are indeed spatially random, we may broaden the class of admissible masks to also include non-random patterns. We shall expand on this point in due course.

[3]This can be true because either (i) the patterns have been previously measured, or (ii) the patterns may be calculated since the structure of both the mask and the illumination has been sufficiently precisely characterized.

scale present in the speckles to a non-negligible degree. The key strategy of ghost projection is to *select a suitable set of mask translations and corresponding exposure times, such that an arbitrary distribution of integrated radiant exposure is indeed registered over the illumination plane* [1–3].

We close this introduction with a brief overview of the remainder of the paper. Section 2 outlines the methods that underpin our experimental demonstration of a universal hard-X-ray mask based on the ghost-projection concept. Section 3 presents our experimental results. Some broader implications of this work are discussed in Section 4, followed by concluding remarks in Section 5.

2. Methods

X-ray ghost projection experiments were carried out at the BM05 beamline of the European Synchrotron Radiation Facility (ESRF) in Grenoble, France. A Si-111 double-crystal monochromator was employed with liquid-nitrogen cooling, giving a relative energy spread $\Delta E/E$ of 10^{-4}. Two different detection modes were used for the experiment: (i) a Maxipix digital photon-counting detector with 55 μm pixel pitch [27], and (ii) X-ray film with an effective grain size of 5μm. Supplement 1 Section 3 contains further details on these two ghost-projection detection modes.

For the Maxipix-based experiments, our procedure consisted of raster scanning our universal mask and imaging the resulting set of patterned illuminations using the pixel detector. All mask-to-detector distances Δ were on the order of 10 mm. This raster scanning was done with a monochromated X-ray beam of energy 23 keV and, separately, 18 keV. Electronic shuttering was employed with better than 1 μs accuracy. The total of N images collected were then used to calculate sets of mask positions and exposure times that would generate specific target GP images; the algorithm is detailed below. The horizontal mask translation stage employed had greater than 0.1 μm repeatability, while the vertical stage had better than 3 μm repeatability.

Adapting these experiments to film-based detection involved (i) the installation of a physical shutter to replace the electronic shutter of the Maxipix detector, and (ii) reducing exposure times by a factor of 10 such that the dose deposition lay within the dynamic range of the film. The physical shutter was a newly-developed ESRF in-house model with open/close time of less than 30 ms [28]. Aluminum attenuators were used to tune the flux to an acceptable level for both the Maxipix detector and film (2.58 mm and 4.47 mm Al, respectively). Note that the mask was in the same position for both setups. This second set of experiments provided a clear demonstration of capability to deposit dose in a structured way on a physical object (*i.e.*, the X-ray film).

The structured illumination patterns were generated using binary attenuation masks. Binary masks are both simpler to fabricate and provide a better GP signal-to-noise ratio due to their maximum variance [29,30]. A range of mask patterns were designed to exhibit specific properties. Specific mask designs employed here include random binary masks with different feature sizes, together with random fractal-like masks with multiscale capabilities, and a non-random mask that forms an orthogonal basis under translation. The various types of mask were written onto a single wafer, with the ghost-projection optimization being allowed to select particular patterns from the different types of mask. A mathematical description of each type of mask is given in Supplement 1 Section 4.

Our binary attenuation masks were constructed through gold (Au) electroplating on a 4-inch diameter glass (SiO_2) substrate with a thickness of 700 μm. The fabrication process is described in detail in Supplement 1 Section 5. The height of the electroplated mask structure was measured as 26 μm within a 4% tolerance, as expected. At 23 keV, X-ray transmission through 26 μm of Au is less than 8% and the X-ray transmission is almost zero at 18 keV. See Fig. 2 for radiographs of the five classes of fabricated binary masks employed in our GP experiments.

The procedure, to convert the mask measurements into an implementable ghost projection scheme, began with a flux correction applied to the mask measurements to normalize the

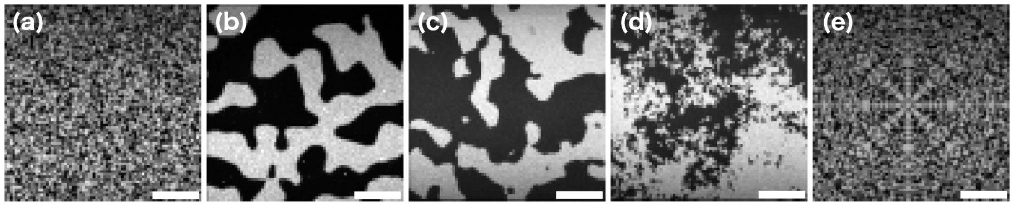

Fig. 2. Universal masks employed for ghost projection using hard X rays: (a) random binary mask, (b) binarized Gaussian-smoothed-noise mask, (c) binarized Lorentzian-smoothed-noise mask, (d) random-fractal mask, (e) Legendre mask. Scale bar, in all panels, is 1 mm.

synchrotron storage ring current to 200 mA. We decided on this approach because, while normalization on the Maxipix could easily be carried out in post-processing, the film exposure requires this correction to be done in real-time. Further, a relative normalization of the masks was applied according to the maximum photon count to ensure easy interpretation and scaling of the final exposures obtained. Next, the two-dimensional mask images R_{ij} were vectorized, mean corrected, and collated into a single matrix, M, as follows:

$$M = [R_{ij1} - \overline{R_{ij1}}; R_{ij2} - \overline{R_{ij2}}; \cdots ; R_{ijN} - \overline{R_{ijN}}]. \tag{1}$$

Here the integers subscripts (i, j) are pixel coordinates; the final subscript k in R_{ijk} denotes the kth image in the sequence of N total images; an overline denotes the statistical average over the free indices (*e.g.*, $\overline{R_{ij1}}$ is the spatial average over the pixel coordinates of the first mask). With this notation in place, we express GP as the linear algebra problem:

$$M\vec{w} \to \vec{I}. \tag{2}$$

Here $\vec{I}$ is the zero-mean, contrast-normalized, vectorized version of our target image; an overhead arrow denotes a vectorized quantity. From this point, we can determine the scheme weights w_k via a number of methods: correlation values, correlation filtration, non-negative least squares optimization, L1-norm minimization with non-negative regularization, *etc*. (as explored in Ref. [2]). Here we used the non-negative least squares (NNLS) optimizer from `MATLAB` to solve for the weights

$$\arg\min \|M\vec{w} - \vec{I}\|, \text{ subject to } w_k \geq 0, \tag{3}$$

where the latter constraint enforces that the exposures remain physical.

As mentioned above, this scheme will produce a pedestal having a uniform exposure equal to $N'\overline{w_k}\overline{R_{ijk'}}$, in units of image contrast. Note that a certain pedestal can be enforced by removing the mean correction in Eq. (1), and then adding the desired value (in units of image contrast) to the right-hand side of Eq. (2). Here $\overline{R_{ijk'}}$ is the average transmission value of the selected N' masks (k is used to index the ensemble of N masks, and k' denotes those selected for the particular target ghost-projection image). These non-negative weights are rescaled to give per-mask exposure times according to the application at hand.[4] A ghost projection is then obtained simply by recalling the locations of the N' selected masks and exposing them for the predetermined period of time (with the aforementioned on-the-fly flux correction to a ring current of 200 mA).

[4]We rescale the maximum expected Maxipix photon count to be within a comfortable margin of its maximum value. For the X-ray film, we scale the integrated exposure time to a predetermined value.

3. Results

Figure 3 gives an experimental demonstration, of the construction of a desired image through the ghost-projection process, using 23 keV X rays. See Visualization 1 for the corresponding video. Using transversely-displaced non-configurable mask patterns similar to Fig. 3(a), with varying illumination times for each selected transverse position, over time the cumulative exposures such as those in Figs. 3(b)-3(e) will eventually integrate to the designed ghost projection, namely the letters "GP" in Fig. 3(f). A total of $N' = 820$ frames was employed in this Maxipix-based, hard-X-ray ghost projection, selected from a total pool of $N = 17\,280$ frames that were captured prior to performing the ghost projection. A random-fractal mask was used for the first 751 frames of this ghost projection, with a binarized Lorentzian-smoothed noise-mask being used for the remaining frames. Exposure times T for individual illumination frames varied between $T_{\text{min}} = 1.01$ ms and $T_{\text{max}} = 118$ ms, with mean $\overline{T} = 20.1$ ms and standard deviation $\sigma_T = 17.3$ ms. For further details, see Supplement 1 Section 6.

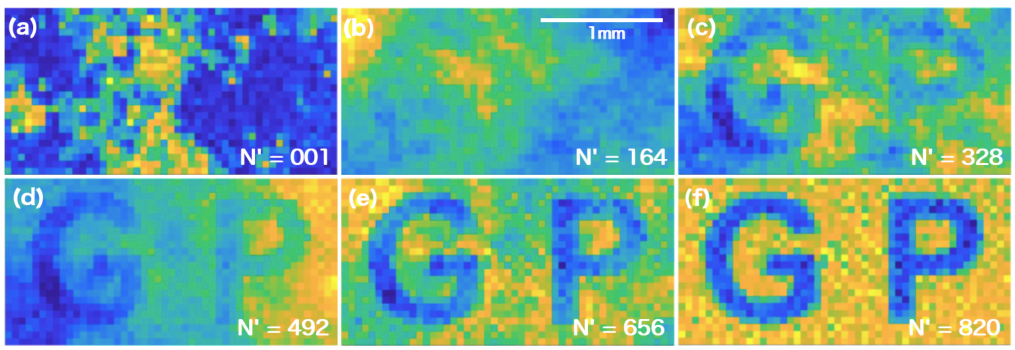

Fig. 3. A subset of the sequence of cumulative ghost-projection exposures in a 25×50 pixel frame, at an X-ray energy of 23 keV, using a digital photon-counting detector. (a) First frame in the sequence, (b) sum of the first 164 frames, (c) sum of the first 328 frames, (d) sum of the first 492 frames, (e) sum of the first 656 frames, and (f) sum of all 820 frames. For all frames in the sequence, see the video in Visualization 1.

To demonstrate that ghost projection is a universal mask for hard X rays, we projected several different distributions, from the total pool of patterns created using the same set of physical masks. We emphasize that these mask patterns inherently contain none of the desired distributions. Figures 4(a)-4(e) show images of increasing pixel dimensions: (a) a positive-contrast dot, (b) 2 positive- and 2 negative-contrast squares, (c) a negative-contrast smiley face, (d) a positive-contrast smiley face, and (e) a negative-contrast segment of the ESRF logo. Visualization 2, Visualization 3, Visualization 4, Visualization 5, and Visualization 6 show the full sequence of frames in the ghost projections, for each of these digital-detector cases, respectively.

We again refer to Supplement 1 Section 6, for more detail. The number of random masks available to make each ghost projection, the selected number of random masks, the experimentally obtained signal-to-noise Ratio (SNR) and several other relevant parameters are given in Supplement 1 Table S1. The precise definition of SNR is given in Supplement 1 Section 7. A further table giving the breakdown of which mask types were employed to produce each of the digital-detector ghost projections is given in Supplement 1 Table S2. As mentioned earlier, all of the mask types were imprinted on a single wafer, with the ghost-projection optimization algorithm being used to select which masks were employed for each desired pattern of radiant exposure.

Film-based X-ray ghost projections were created using 18 keV radiation, subsequently placing the developed film on a light box and taking visible-light photographs using a Sony Alpha

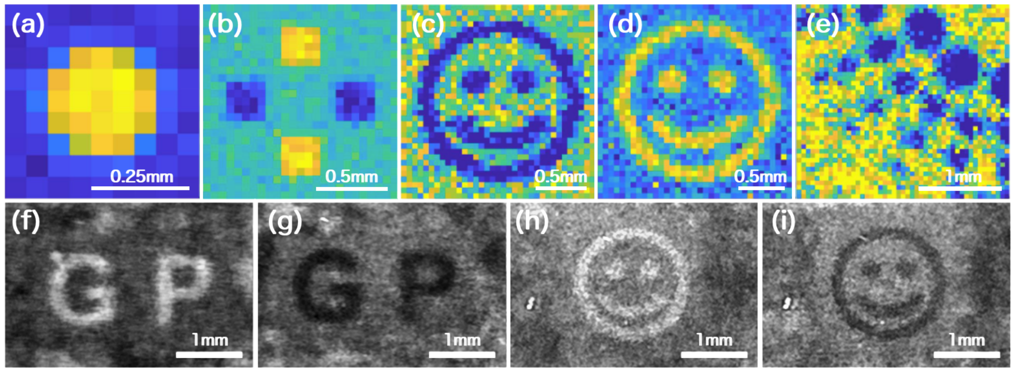

Fig. 4. Example digital-detector (a-e) and film-based (f-i) X-ray ghost projections demonstrating the universality of the scheme to create various images. (a)-(b) utilize a beam energy of 23 keV, while the remainder use a beam energy of 18 keV.

7 Mark II digital camera (24.7 MP CMOS sensor). Note that contrast is reversed on X-ray film. Figures 4(f)-4(h) depict the successfully-produced X-ray ghost-projection patterns: (f) a negative-contrast "GP", (g) a positive-contrast "GP", (h) negative-contrast smiley face, and (i) a positive-contrast smiley face.

4. Discussion

We expand on the anticipated applications motivating our work, which were briefly mentioned in the opening paragraph of Section 1:

1. *Spatial-light-modulator analog, for short-wavelength radiation and matter fields:* When integrated over the time interval needed to create a desired ghost projection (cf. Refs. [31–33]), our method may be viewed as the analog of a spatial light modulator (SLM). It can be applied to short-wavelength radiation and matter fields—such as hard X rays, gamma rays, and neutrons—for which dynamic beam shaping elements do not currently exist with any appreciable spatial resolution. In these regimes, ghost projection has the advantage of experimental simplicity and low cost, relative to strategies which seek to construct direct SLM analogs (*e.g.* with micromirror arrays [34, 35]).

2. *Universal mask for hard X-ray photolithography:* It is challenging to translate conventional photolithographic-mask concepts to the hard X-ray energy range, since (i) at short wavelengths the required aspect ratios for absorptive masks increase to the point where they become mechanically unstable, and (ii) the proximity effect [36–38], associated with Fresnel diffraction in the smallest available mask-to-substrate propagation distances Δ, becomes stronger as feature sizes reduce. This Fresnel contrast mechanism will often be more effective than attenuation for generating high-contrast speckle patterns, *e.g.* in the hard-X-ray and gamma-ray domains. Such propagation-based contrast [39] is therefore an enabling feature of GP, in comparison to conventional methods for short-wavelength mask-based photolithography where the proximity effect is typically detrimental. Demagnifying geometries[5] and raster-scanning geometries may also be employed, in future applications of GP to short-wavelength photolithography. Non-photon lithography, *e.g.* atomic-beam lithography [40, 41], may also be considered from a GP perspective.

[5] See the final paragraph of this section, for more detail on this point.

3. *Universal short-wavelength mask for volumetric additive manufacturing:* Volumetric additive manufacturing [10–13] may be viewed as "tomography in reverse", where a 3D dose-sensitive substrate is illuminated from a variety of angles, to create a desired 3D distribution of radiant exposure such that a desired 3D volume is created when the exposed substrate is subsequently developed. The shorter the illumination wavelength, the finer the feature size that may be written. However, the method is currently limited by the need to employ high-resolution dynamic beam-shaping elements such as spatial light modulators, which do not exist in the X-ray regime. By replacing spatial light modulators with ghost projection, volumetric additive manufacturing using short-wavelength illumination (such as hard X rays) could be achieved (cf. Refs. [1, 42, 43]).

4. *Intensity-modulated radiotherapy and microbeam radiotherapy:* GP might also be of use in shaping specified volumetric distributions of radiant exposure in the context of intensity-modulated radiotherapy [14]. Microbeam radiotherapy [44] might also employ a ghost-projection variant, in which dose is spatially fractionated to separated high-dose volumes within a target area such as a tumor, with relatively low dose elsewhere. Synchrotron-based FLASH radiotherapy [45] might also be amenable to the ghost-projection concept.

We now comment on the role of the additive offset, or pedestal, in the context of GP. As shown by the example of the Hurter-Driffield curve [46] for film, there is a nonlinear relation between (i) the total radiant exposure that illuminates a light-sensitive surface such as a film or photolithographic substrate, and (ii) the response of that surface or material to the illumination. In potential future applications to photolithographic GP, the nonlinearity of the exposure–response relation could be used to advantage. In particular, given the fact that the contrast of a ghost projection may be traded off against its associated pedestal, we can tune this additive offset [2, 3] to match the activation dose (threshold exposure) of a substrate with non-linear response.

For the ghost projections in this experiment, the incident beam was attenuated by at least 96% due to hardware limitations (maximum flux on the detector and maximum operating speed of the fast shutter). Even so, recording one GP required no more than a few minutes. Most of this time was in fact "dead time" during stage movement, so the use of GP in a production environment could benefit from high-speed stages and optimized trajectories. Optimization of the mask-displacement trajectories, for the purposes of GP, is very closely related to the famous traveling-salesperson problem [47] (see [3]). In turn, extension to an optimized shutter-free continuous-exposure GP protocol is equivalent to a continuum generalization of the traveling-salesperson problem.

Another avenue for future work pertains to noise inclusions during the acquisition of the ensemble of masks (*e.g.* Poisson noise, "hot"-pixels, "dead"-pixels, beam-profile fluctuations, *etc*.). In our prior work, we assumed the mask acquisitions could be achieved in a mostly noise-free way and pursued non-negative least squares optimization. During our experiments, however, this proved to be a limiting factor on the final SNR obtained. A study into mask noise inclusions and a more robust GP reconstruction algorithm (such as L1-error minimization with non-negative regularization) would benefit future demonstrations and applications.

Finally, we employed a large-Fresnel-number geometry that yields a direct morphological resemblance, between the projected mask structure and the illumination pattern created by that mask. However, the GP concept is not restricted to such scenarios, as shown in the following two illustrative examples. (i) If a thick spatially-random slab is illuminated with coherent radiation or matter waves, the speckle field at the exit surface of the slab will have an intensity distribution that does not bear a direct resemblance to the morphology of the scattering volume, on account of the influence of multiple scatter [25] (dynamical diffraction [5]) within the volume of the slab. GP methods may be employed nevertheless, if the exit-surface intensity of the mask is either measured or calculable. This would enable the shaping of a desired distribution of time-integrated radiant exposure, at the exit-surface of a thick spatially-random slab, using the ghost-projection concept. (ii) Consider, as a second example, an ensemble of aberrated focal fields, corresponding to a coherently illuminated circular lens whose associated collapsing spherical wave is deformed *e.g.* by a phase distribution given by a suitable linear combination of Zernike circle polynomials [46]. The resulting ensemble of aberrated focal-plane intensity distributions will be highly structured [46, 48] diffraction catastrophes [49], which could be employed as an overcomplete [50] basis for the purposes of ghost projection. Since the diffraction physics of coherent waves in focal regions is very well understood [51], the aberrated focal patterns need not be measured, and could instead be calculated based on the known coherent aberrations [46] of the focusing system. This concept could be employed for focused-beam ghost-projection lithography using controllable-aberration coherent electron [52] or X-ray [53] focused probes. Rather than transversely scanning the probe, as done *e.g.* in electron-beam lithography [54], both the probe and substrate would be stationary, with an ensemble of coherent aberrations being "dialled up" for the probe, in order to create a desired time-integrated ghost-projection distribution of radiant exposure, over a substrate at the focal plane of the probe.

5. Conclusion

An experimental proof of concept was given, for the use of the ghost-projection concept to create a universal mask for hard X rays. This method, which may be viewed as a reversed form of classical computational ghost imaging, may be of relevance for applications such as a spatial light modulator for hard X rays, a universal lithographic mask for short-wavelength irradiation, volumetric additive manufacturing, and various forms of intensity-modulated radiotherapy. While we have focused on the demonstration of ghost projection using X rays, the method may also be used for radiation and matter-wave fields for which dynamical beam-shaping elements either do not exist or have insufficient spatial resolution, such as electrons, neutrons, muons, gamma rays, atomic beams and molecular beams.

Funding

Australian Research Council (ARC) (DP210101312); European Synchrotron (ESRF) (proposal MI-1448).

Acknowledgments

We acknowledge the European Synchrotron Radiation Facility (ESRF) for provision of synchrotron radiation facilities and we would like to thank Mathieu Manni and Nicola Viganò for assistance and support in using beamline BM05. We are grateful for useful discussions with Lindon Roberts and Wilfred Fullagar. This work was performed in part at the Melbourne Centre for Nanofabrication (MCN) in the Victorian Node of the Australian National Fabrication Facility (ANFF).

Disclosures

The authors declare no conflicts of interest.

Data availability

The data that support the images within this paper and other findings of this study have been stored on the mass data storage system (MDSS) at the Australian National Computational Infrastructure (NCI, nci.org.au) and are available from the corresponding author upon reasonable request. DOI for all data collected: 10.15151/ESRF-ES-955501848.

Supplemental document

See Supplement 1 for supporting text.

Supplemental media

See Visualization 1, Visualization 2, Visualization 3, Visualization 4, Visualization 5, and Visualization 6 for supporting videos.

VISUALIZATION 1:
https://opticapublishing.figshare.com/s/4d0ca8381d2a1070f4cf
VISUALIZATION 2:
https://opticapublishing.figshare.com/s/ba108e9dff9fcadd86ab
VISUALIZATION 3:
https://opticapublishing.figshare.com/s/5975b0239d3398b6fb79
VISUALIZATION 4:
https://opticapublishing.figshare.com/s/c4048dbcff56f03bfaf1
VISUALIZATION 5:
https://opticapublishing.figshare.com/s/bf6a2562b18e1f7891d0
VISUALIZATION 6:
https://opticapublishing.figshare.com/s/9e8da8b7fc44f36f5938

References

1. D. M. Paganin, "Writing arbitrary distributions of radiant exposure by scanning a single illuminated spatially random screen," Phys. Rev. A **100**, 063823 (2019).
2. D. Ceddia and D. M. Paganin, "Ghost projection," Phys. Rev. A **105**, 013512 (2022).
3. D. Ceddia, A. M. Kingston, D. Pelliccia, A. Rack, and D. M. Paganin, "Ghost projection. II. Beam shaping using realistic spatially random masks," Phys. Rev. A **106**, 033512 (2022).
4. M. Utsuro and V. K. Ignatovich, *Handbook of Neutron Optics* (Wiley VCH Verlag GmbH, Weinheim, 2010).
5. J. M. Cowley, *Diffraction Physics* (Elsevier, Amsterdam, 1995), 3rd ed.
6. L. Cimmino, F. Ambrosino, A. Anastasio, M. D'Errico, V. Masone, L. Roscilli, and G. Saracino, "A new cylindrical borehole detector for radiographic imaging with muons," Sci. Rep. **11**, 17425 (2021).
7. S. Yamamoto, K. Ninomiya, N. Kawamura, and Y. Hirano, "Optical imaging of muons," Sci. Rep. **10**, 20790 (2020).
8. H. J. Metcalf and P. van der Straten, *Laser Cooling and Trapping* (Springer, New York, 1999).
9. D. C. Joy, *Helium Ion Microscopy: Principles and Applications* (Springer, New York, 2013).
10. M. P. de Beer, H. L. van der Laan, M. A. Cole, R. J. Whelan, M. A. Burns, and T. F. Scott, "Rapid, continuous additive manufacturing by volumetric polymerization inhibition patterning," Sci. Adv. **5**, eaau8723 (2019).
11. B. E. Kelly, I. Bhattacharya, H. Heidari, M. Shusteff, C. M. Spadaccini, and H. K. Taylor, "Volumetric additive manufacturing via tomographic reconstruction," Science **363**, 1075–1079 (2019).
12. D. Loterie, P. Delrot, and C. Moser, "High-resolution tomographic volumetric additive manufacturing," Nat. Commun. **11**, 852 (2020).
13. J. T. Toombs, M. Luitz, C. C. Cook, S. Jenne, C. C. Li, B. E. Rapp, F. Kotz-Helmer, and H. K. Taylor, "Volumetric additive manufacturing of silica glass with microscale computed axial lithography," Science **376**, 308–312 (2022).
14. B. Cho, "Intensity-modulated radiation therapy: a review with a physics perspective," Radiat. Oncol. J. **36(1)**, 1–10 (2018).
15. J. H. Shapiro, "Computational ghost imaging," Phys. Rev. A **78**, 061802 (2008).
16. B. I. Erkmen and J. H. Shapiro, "Ghost imaging: from quantum to classical to computational," Adv. Opt. Photonics **2**, 405–450 (2010).
17. J. H. Shapiro and R. W. Boyd, "The physics of ghost imaging," Quantum Inf. Process. **11**, 949–993 (2012).
18. M. J. Padgett and R. W. Boyd, "An introduction to ghost imaging: quantum and classical," Phil. Trans. R. Soc. A **375**, 20160233 (2017).
19. D. Pelliccia, M. P. Olbinado, A. Rack, A. M. Kingston, G. R. Myers, and D. M. Paganin, "Towards a practical implementation of X-ray ghost imaging with synchrotron light," IUCrJ **5**, 428–438 (2018).
20. D. Ceddia and D. M. Paganin, "Random-matrix bases, ghost imaging, and x-ray phase contrast computational ghost imaging," Phys. Rev. A **97**, 062119 (2018).
21. T. E. Gureyev, D. M. Paganin, A. Kozlov, Ya. I. Nesterets, and H. M. Quiney, "On the efficiency of computational imaging with structured illumination," Phys. Rev. A **97**, 053819 (2018).
22. Y. Bromberg, O. Katz, and Y. Silberberg, "Ghost imaging with a single detector," Phys. Rev. A **79**, 053840 (2009).
23. O. Katz, Y. Bromberg, and Y. Silberberg, "Compressive ghost imaging," Appl. Phys. Lett. **95**, 131110 (2009).

24. D. M. Paganin, *Coherent X-Ray Optics* (Oxford University Press, Oxford, 2006).
25. A. P. Mosk, A. Lagendijk, G. Lerosey, and M. Fink, "Controlling waves in space and time for imaging and focusing in complex media," Nat. Photonics **6**, 283–292 (2012).
26. C. Zhang, Y. Xin, and X. Zhu, "Multiscale and local engineering of speckle morphology through disordered media," Opt. Lett. **47**, 6029–6032 (2022).
27. C. Ponchut, J. M. Rigal, J. Clément, E. Papillon, A. Homs, and S. Petitdemange, "MAXIPIX, a fast readout photon-counting X-ray area detector for synchrotron applications," J. Inst. **6**, C01069 (2011).
28. C. Muñoz Pequeño, J. M. Clement, P. Thevenau, and P. Van Vaerenbergh, "Development of a linear fast shutter for BM05 at ESRF and BEATS at SESAME," in *Proc. MEDSI'20,* (JACoW Publishing, Geneva, Switzerland, 2021), 11, pp. 229–231.
29. A. M. Kingston, W. K. Fullagar, G. R. Myers, D. Adams, D. Pelliccia, and D. M. Paganin, "Inherent dose-reduction potential of classical ghost imaging," Phys. Rev. A **103**, 033503 (2021).
30. A. M. Kingston, A. Aminzadeh, L. Roberts, D. Pelliccia, I. D. Svalbe, and D. M. Paganin, "Optimizing nonconfigurable, transversely displaced masks for illumination patterns in classical ghost imaging," Phys. Rev. A **107**, 023524 (2023).
31. A. Boccolini, A. Fedrizzi, and D. Faccio, "Ghost imaging with the human eye," Opt. Express **27**, 9258–9265 (2019).
32. G. Wang, H. Zheng, Z. Tang, Y. Zhou, H. Chen, J. Liu, Y. He, Y. Yuan, F. Li, and Z. Xu, "All-optical naked-eye ghost imaging," Sci. Rep. **10**, 2493 (2020).
33. G. Wang, H. Zheng, Z. Tang, Y. He, Y. Zhou, H. Chen, J. Liu, Y. Yuan, F. Li, and Z. Xu, "Naked-eye ghost imaging via photoelectric feedback," Chin. Opt. Lett. **18**, 091101 (2020).
34. Y. Shroff, Y. Chen, and W. Oldham, "Fabrication of parallel-plate nanomirror arrays for extreme ultraviolet maskless lithography," J. Vac. Sci. Technol. B **19**, 2412–2415 (2001).
35. N. Chkhalo, V. Polkovnikov, N. Salashchenko, and M. Toropov, "Deposition of Mo/Si multilayers onto MEMS micromirrors and its utilization for extreme ultraviolet maskless lithography," J. Vac. Sci. Technol. B **35**, 062002 (2017).
36. Y. Vladimirsky, A. Bourdillon, O. Vladimirsky, W. Jiang, and Q. Leonard, "Demagnification in proximity x-ray lithography and extensibility to 25 nm by optimizing Fresnel diffraction," J. Phys. D: Appl. Phys. **32**, L114–L118 (1999).
37. A. J. Bourdillon, C. B. Boothroyd, J. R. Kong, and Y. Vladimirsky, "A critical condition in Fresnel diffraction used for ultra-high resolution lithographic printing," J. Phys. D: Appl. Phys. **33**, 2133–2141 (2000).
38. A. J. Bourdillon and C. B. Boothroyd, "Proximity correction simulations in ultra-high resolution x-ray lithography," J. Phys. D: Appl. Phys. **34**, 3209–3213 (2001).
39. A. Snigirev, I. Snigireva, V. Kohn, S. Kuznetsov, and I. Schelokov, "On the possibilities of x-ray phase contrast microimaging by coherent high-energy synchrotron radiation," Rev. Sci. Instrum. **66**, 5486–5492 (1995).
40. D. Meschede and H. Metcalf, "Atomic nanofabrication: atomic deposition and lithography by laser and magnetic forces," J. Phys. D: Appl. Phys. **36**, R17–R38 (2003).
41. C. S. Allred, J. Reeves, C. Corder, and H. Metcalf, "Atom lithography with metastable helium," J. Appl. Phys. **107**, 033116 (2010).
42. A. M. Kingston, D. Pelliccia, A. Rack, M. P. Olbinado, Y. Cheng, G. R. Myers, and D. M. Paganin, "Ghost tomography," Optica **5**, 1516–1520 (2018).
43. A. M. Kingston, G. R. Myers, D. Pelliccia, I. D. Svalbe, and D. M. Paganin, "X-ray ghost-tomography: Artefacts, dose distribution, and mask considerations," IEEE Trans. Comput. Imaging **5**, 136–149 (2019).
44. M. A. Grotzer, E. Schültke, E. Bräuer-Krisch, and J. A. Laissue, "Microbeam radiation therapy: Clinical perspectives," Phys. Medica **31**, 564–567 (2015).
45. M.-C. Vozenin, J. Bourhis, and M. Durante, "Towards clinical translation of FLASH radiotherapy," Nat. Rev. Clin. Oncol. **19**, 791–803 (2022).
46. M. Born and E. Wolf, *Principles of Optics* (Cambridge University Press, Cambridge, 1999), 7th ed.
47. R. S. Armour and J. A. Wheeler, "Physicist's version of traveling salesman problem: statistical analysis," Am. J. Phys. **51**, 405–406 (1983).
48. S. W. Paine and J. R. Fienup, "Machine learning for improved image-based wavefront sensing," Opt. Lett. **43**, 1235–1238 (2018).
49. Yu. A. Kravtsov and Yu. I. Orlov, *Caustics, Catastrophes and Wave Fields* (Springer, Berlin, 1999), 2nd ed.
50. L. Mandel and E. Wolf, *Optical Coherence and Quantum Optics* (Cambridge University Press, Cambridge, 1995).
51. J. J. Stamnes, *Waves in Focal Regions* (Taylor & Francis, New York, 1986).
52. A. Kallepalli, L. Viani, D. Stellinga, E. Rotunno, R. Bowman, G. M. Gibson, M.-J. Sun, P. Rosi, S. Frabboni, R. Balboni, A. Migliori, V. Grillo, and M. J. Padgett, "Challenging point scanning across electron microscopy and optical imaging using computational imaging," Intell. Comput. **2022**, 0001 (2022).
53. T. Kimura, S. Matsuyama, K. Yamauchi, and Y. Nishino, "Coherent x-ray zoom condenser lens for diffractive and scanning microscopy," Opt. Express **21**, 9267–9276 (2013).
54. Y. Chen, "Nanofabrication by electron beam lithography and its applications: A review," Microelectron. Eng. **135**, 57–72 (2015).

Universal mask for hard X rays: Supplementary information

This supplement provides supporting information for the main text of our paper. Section 1 gives an abstract description of the ghost-projection concept, by linking it to the linear-algebra question of decomposing a given high-dimensional vector in terms of a superposition of random vectors. Section 2 compares classical ghost imaging and ghost projection, with the latter being viewed as a reversed or inverted form of the former. The digital-detector and film-based experimental X-ray detection modes, employed in the main text of the paper, are described in Section 3. Section 4 covers the classes of ghost-projection mask design that were employed in our X-ray ghost-projection experiments. Associated details regarding mask fabrication are given in Section 5. Section 6 gives additional descriptive details and experimental parameters regarding the ghost-projection images in the main text of the paper. Section 7 explains how the signal-to-noise ratio of the experimental X-ray ghost projections was calculated. Finally, Section 8 describes the ghost-projection videos that accompany this paper.

1. ABSTRACT DESCRIPTION OF GHOST PROJECTION

Consider a large number of random vectors having no preferred direction, the tails of which are all fixed to a given point that is specified to be the origin of coordinates. To approximate any desired vector as a linear combination of these random vectors, we can (i) discard every random vector that has a negative projection with respect to the desired vector, before (ii) subsequently summing the vectors that remain, and then (iii) multiplying by a suitable positive constant. More efficient vector-selection schemes could of course be chosen, but the key in-principle concept is clear, namely that random vectors form a mathematical basis [1]. This geometrically-framed idea works in any number of dimensions, so we can consider our vector space to be a high-dimensional function space. Each vector, in this high-dimensional space, may be associated with a distinct image [2]. Suppose, now, that each axis of this function space corresponds to a linearly-independent two-dimensional noise map ("speckle field"), such as might be produced by transversely scanning a spatially-random screen. We immediately conclude that an arbitrary image—or, stated more precisely, an arbitrary time-integrated spatial distribution of radiant exposure—may be synthesized by transversely scanning a spatially-random illuminated screen [3–5]. Clearly, the arbitrariness of this "ghost projection" image is up to a spatial resolution dictated by the finest features present in the patterned illumination. Also, there will be an additive offset ("pedestal") in the projected pattern, since intensity measurements can never be negative. See Fig. 1(a) of the main paper, for a schematic indication of these enabling concepts.

2. COMPARISON OF GHOST PROJECTION WITH GHOST IMAGING

The notion of ghost projection [3–5] may be viewed as a reversed form of computational classical ghost imaging [6–8]. In the latter technique, the intensity–intensity correlations ("bucket" signals) between predetermined illumination masks and an unknown illuminated object are employed, in order to calculate an image of that object. In the former technique, intensity correlations are established over the ghost-projection plane, rather than being measured via a bucket detector. Both positive and negative correlations may be established, as we have already seen in our ability to generate patterns with both positive and negative contrast relative to the ghost-projection pedestal (see Fig. 4(b) in the main paper). As another interesting point of comparison, in classical ghost imaging, no photon that passes through the sample is ever measured by a position-sensitive detector; this may be compared to the fact that, in ghost projection, no imaging quantum ever passes through a precisely-constructed beam-shaping element, in order to create a desired spatial distribution of radiant exposure.

While ghost projection may be viewed as a reversed form of classical computational ghost imaging, the role of prior knowledge is very different. For ghost imaging with random masks in the absence of any prior knowledge regarding the sample, a relatively large number of bucket measurements needs to be taken, on account of the random-mask basis being non-optimal in comparison to complete orthogonal-basis mask sets. In the presence of suitable prior knowledge regarding the sample, the number of required bucket measurements may be reduced (in classical computational ghost imaging), thereby decreasing the data-acquisition time and reducing the dose to the sample. For ghost projection, however, we necessarily have total prior knowledge regarding the particular image that we wish to ghost project. This enables us to select a very small fraction of our masks, in order to generate a ghost projection using relatively few masks. Importantly, if two or more independently-translatable random masks are illuminated in series[1], the number of possible random masks in the resulting overcomplete [9] basis is exponentially large [4, 5]. This allows us to choose an extremely small fraction of the possible random masks, enabling an efficient ghost projection with far fewer masks than would be needed if we worked with a particular specified set of orthogonal masks which all needed to be used. Returning to the "sheaf of random vectors" [3, 4] concept in Section 1 of this Supplement, the ability to discard most random vectors allows us to work with a chosen subset that enables particularly efficient ghost projection (cf. Ref. [10]). Comparisons with compressed sensing are natural, in this context [11–13]. *Ghost projection has total prior knowledge of the image to be projected*, a situation having no direct analog in ghost imaging. This complete prior knowledge implies that the question of optimal mask choice is different for computational ghost imaging and ghost projection. A variety of masks can be employed in either case, such as random binary masks, random fractal masks, uniformly redundant arrays, and masks based on the finite Radon transform [14]. It would be interesting to investigate which class of mask is most appropriate for particular ghost-projection applications, in future explorations of the method. In a similar vein, while we have employed non-negative least squares as the means by which the illuminated subset of possible masks is chosen, the use of more sophisticated computational optimization approaches will likely make the process more efficient.

3. EXPERIMENTAL DETECTION MODES

Two different detection modes were used for the X-ray ghost-projection experiments:

Maxipix: A digital photon-counting pixel detector developed at ESRF, Maxipix (Multichip Area X-ray detector based on a photon-counting PIXel array) [15]. The Maxipix has a 1260×256 pixel array with a pixel pitch of 55 µm.

X-ray film: Structurix D3-SC industrial X-ray film (Agfa-Gevaert Group; Mortsel, Belgium). The film was processed using an Industrex M37 plus Processor (Colenta Labortechnik GmbH; Wiener Neustadt, Austria) with XR D-6 NDT developer and XR F-6 NDT fixer solutions (Duerr NDT; Bietigheim-Bissingen, Germany). The film has a 3 µm physical grain size. The effective grain size is 5µm, considering errors from exposure, developing, and digitization.

4. MASK DESIGN

The following three classes of mask were employed for our ghost-projection experiments, with further details available in Ref. [14] in a classical-ghost-imaging context. Note that, in the experiments reported in the main paper, all of the following types of mask were written on a single wafer.

- *Random binary masks* $\mathcal{A}$ correspond to binary random noise on a pixelated array of contiguous square plaquettes, with each of two different transmission values at each pixel being equally likely. The random transmission coefficient for each pixel is statistically independent of every other pixel, by construction.

- *Binarized Gaussian-smoothed noise masks* $\mathcal{B}_\sigma$ correspond to convolving $\mathcal{A}$ with a Gaussian function of specified full width at half maximum (FWHM), equal to $2\sqrt{2\ln 2}\sigma$ pixels, and then binarizing the resulting array.

- *Binarized Lorentzian-smoothed noise masks* $\mathcal{C}_\gamma$ correspond to convolving $\mathcal{A}$ with a Lorentzian function of specified FWHM, equal to 2γ pixels, and then binarizing the resulting array.

- *Random-fractal masks* $\mathcal{D}_{\alpha,\beta}$ correspond to convolving $\mathcal{A}$ with a suitable filter kernel, followed by binarization. The filter kernel, for this approximately self-similar mask [16], has the Fourier-space form

$$H(k_x, k_y) = \frac{1}{(k_x^2 + k_y^2)^{\alpha/2} + \beta}. \tag{S1}$$

[1]As pointed out in Ref. [4], this idea was proposed by Kaye S. Morgan (Monash University, Australia) in the context of ghost projection, in a private communication to DC and DMP on June 24, 2021.

Here, (k_x, k_y) denote discrete spatial frequencies in each of two transverse dimensions [17], $\alpha \geq 0$ is a critical exponent [18] that governs the power-law decay of the fractal-mask power spectrum at large spatial frequencies, and β is a small real regularization parameter which mollifies the blowup that would otherwise occur at the Fourier-space origin $(k_x, k_y) = (0, 0)$. The special case $\alpha = 2$ corresponds to a Lorentzian function.

- *Legendre masks* $\mathcal{E}_p$ corresponds to a 2D $p \times p$ pattern, constructed from the finite Radon transform, that is orthogonal under translation. This mask is defined in Ref. [19].

The classes of universal mask employed for ghost projection using hard X-rays (as depicted in Fig. 2 in the main text of the paper) are as follows: (a) random binary mask $\mathcal{A}$, (b) binarized Gaussian-smoothed-noise mask $\mathcal{B}_\sigma$ ($\sigma = 8.5$ pixels), (c) binarized Lorentzian-smoothed-noise mask $\mathcal{C}_\gamma$ ($\gamma = 14.14$ pixels), (d) random-fractal mask $\mathcal{D}_{\alpha,\beta}$ ($\alpha = 1$, β= 0), (e) Legendre mask $\mathcal{E}_p$, $p = 127$.

5. MASK FABRICATION

The attenuation ghost-projection masks were fabricated on a 4-inch SiO_2 substrate (wafer) with 700 µm thickness. The fabrication process was mainly carried out at the Melbourne Centre for Nanofabrication (MCN) in Melbourne, Australia. The substrate was first cleaned with piranha solution to remove organic residues and then coated with 20 nm of Cr followed by 100 nm of Au using an Intlvac Nanochrome sputtering machine. The Cr layer was used as an adhesion layer because the adhesion between SiO_2 and Au is weak. The Au layer was used as a conductive layer for the subsequent electroplating. After the sputtering process, the wafer was spin-coated with an AZ 40XT-11D positive photoresist and baked at 126 degrees for 5 minutes. The thickness of the photoresist was measured as approximately 40 µm using an optical profilometer (Bruker Contour GT-I). This thickness is sufficient to obtain 20 to 30 µm electroplated structures. Our mask patterns were then transferred from a Cr mask into the photoresist under UV light exposure and through a photolithography process (using the EVG6200 mask aligner instrument). The exposed wafer was baked at 105 degrees for 90 seconds before it was developed in an AZ 726 solution for 5 minutes. In the last step of the fabrication process, Au electroplating was performed in a Pur-A-Gold 402 solution (trademark Macdermid-Enthone) for 90 minutes. The height of the electroplated mask structures was measured as 26 µm within a 4% tolerance, as expected.

6. DETAILS OF EXAMPLE GHOST-PROJECTION IMAGES

The cumulative exposures in the first ghost experimental X-ray projection, as presented in Fig. 3 of the main text of the paper, is reproduced along with additional numerical parameters (scale bars indicating photon counts, and additional detail in the caption) in Fig. S1 below.

We now give additional information regarding the X-ray ghost projections in Fig. 4 from the main text of the paper. This additional detail is given in Fig. S2 below. From a given set of random masks, we projected, in order of increasing total pixels:

- a 10×10 pixel image of a dot, using the Maxipix detector (Fig. S2a);
- a 26×26 pixel image containing two “up” dots and two “down” dots, where “up” and “down” refer to regions of relatively high and low dose, respectively, using the Maxipix detector (Fig. S2b);
- a 25×50 pixel image of the initials “GP”, defined by a region of relatively low dose, using the Maxipix detector (Fig. S2c) and film (Fig. 4(f) in the main paper);
- an “inverse GP” image on film, Fig. 4(g) in the main paper, where by “inverse”, we mean that the regions of relatively high exposure are inverted to relatively low, and vice versa;
- a 36×36 pixel image of a smiley face defined by a region of relatively low dose using the Maxipix detector (Fig. S2d), and on film (Fig. 4(h) in the main paper);
- an inverse smiley distribution on the Maxipix detector (Fig. S2e) and on film (Fig. 4(i) in the main paper);
- a 44×48 pixel image of one-quarter of the ESRF’s logo dots (Fig. S2f).

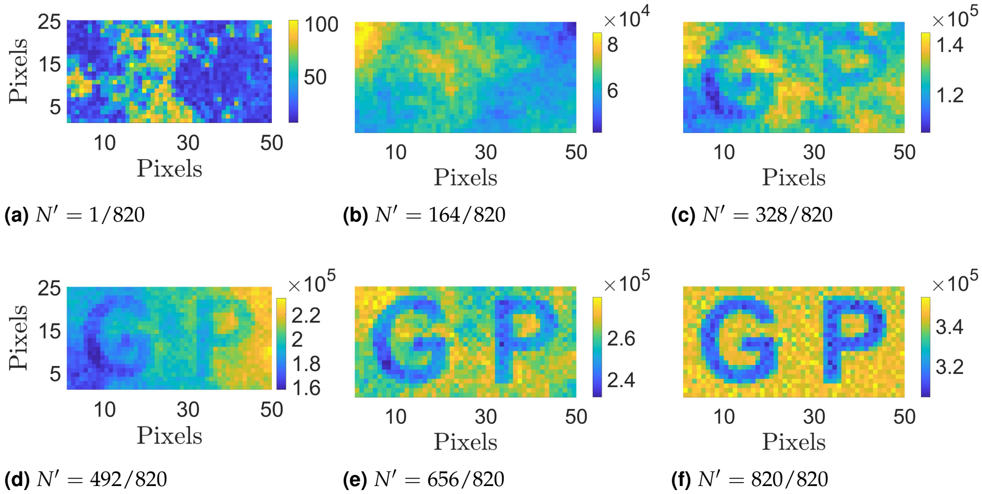

Fig. S1. Sequence of cumulative 23 keV X-ray ghost-projection exposures in a 25×50 pixel frame (units of photon counts). Maxipix pixel pitch is 55 µm. The video in Visualization 1 shows the full sequence of $N' = 820$ frames that were selected from a total pool of $N = 17\,280$ frames, for both (i) the N'th random-mask image in the exposure and (ii) the cumulative exposure for the first N' masks.

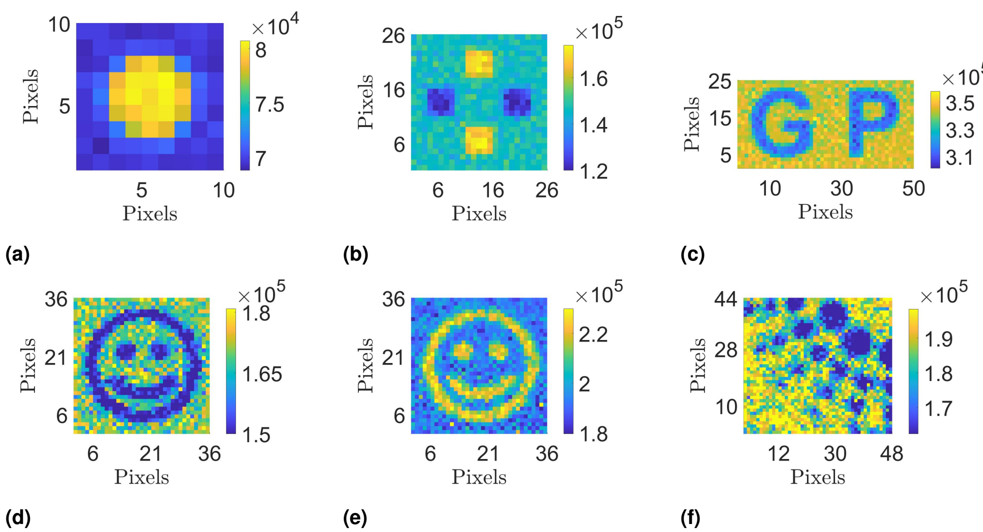

Fig. S2. Maxipix X-ray ghost projections, expressed in photon counts, demonstrating the universality of the scheme to create varied projections, in order of increasing number of pixels. (a)-(c) are X-ray ghost projections with beam energy 23 keV, (d)-(f) use a beam energy of 18 keV. Associated videos show the full sequence of frames in the ghost projections for the respective panels: (a) Visualization 2, (b) Visualization 3, (d) Visualization 4, (e) Visualization 5, and (f) Visualization 6. Each video shows (i) each random-mask image in the exposure and (ii) the cumulative exposure. Additional relevant parameters are given in Table S1 and Table S2.

7. DETERMINATION OF SIGNAL-TO-NOISE RATIO

The signal-to-noise ratio (SNR) of each Maxipix-based GP result was determined by first calculating the variance. In particular, the variance of the experimental ghost projection P was estimated by subtracting the average (pedestal, $\overline{P}$), i.e., $P' = P - \overline{P}$, and rescaling the result to have a consistent standard deviation with the target image, I. The target image was then subtracted, the

Table S1. Key parameters associated with the six Maxipix-based X-ray ghost projections, in Fig. 3(f) and 4(a-e) from the main paper. In the left column, we use the following abbreviations: "No."="number", "Exp."="exposure time", "SD"="standard deviation", and "SNR"="signal-to-noise ratio".

Image	Fig. 3(f)	Fig. 4(a)	Fig. 4(b)	Fig. 4(c)	Fig. 4(d)	Fig. 4(e)
No. Pixels	1250	100	676	1296	1296	2112
No. Available Masks	17 280	484	5 760	35 574	35 574	29 645
No. Selected Masks	820	92	265	490	462	388
Mean Exp. (ms)	20.1	33.0	23.0	18.5	24.0	26.2
SD Exp. (ms)	17.3	27.4	20.6	17.4	23.3	25.2
Max Exp. (ms)	118	167	125	136	136	136
Min Exp. (ms)	1.01	1.19	1.07	0.07	0.18	0.27
Experimental SNR	3.01	5.04	2.44	1.56	1.71	1.16

result squared, and the pixels were summed over in the usual way:

$$\mathrm{Var}[P'] = \mathrm{E}\left[\left(P'\sqrt{\frac{\mathrm{E}[I^2]}{\mathrm{E}[P'^2]}} - I\right)^2\right]. \tag{S2}$$

Combining this with the signal of the target image (ignoring the pedestal), $\mathrm{E}[I^2]$, this gave the SNR as:

$$\mathrm{SNR} = \sqrt{\frac{\mathrm{E}[I^2]}{\mathrm{Var}\,[P']}}. \tag{S3}$$

8. MEDIA FILES

Here we describe the ghost-projection videos that accompany our paper. In each of these videos, the left panel shows the individual Maxipix exposures that make up a given ghost projection, with the cumulative digital-detector exposure given in the right frame.

- Visualization 1 corresponds to the "GP" image shown in Fig. 3 of the main paper, together with the more detailed version in Fig. S1 and Fig. S2(c) of this Supplement. https://opticapublishing.figshare.com/s/4d0ca8381d2a1070f4cf
- Visualization 2 corresponds to Fig. 4(a) in the main paper (positive-contrast dot), together with the more detailed version in Fig. S2(a) of this Supplement. https://opticapublishing.figshare.com/s/ba108e9dff9fcadd86ab
- Visualization 3 corresponds to Fig. 4(b) in the main paper (2 positive-contrast and 2 negative-contrast squares), together with the more detailed version in Fig. S2(b) of this Supplement. https://opticapublishing.figshare.com/s/5975b0239d3398b6fb79
- Visualization 4 corresponds to Fig. 4(c) in the main paper (negative-contrast smiley face), together with the more detailed version in Fig. S2(d) of this Supplement. https://opticapublishing.figshare.com/s/c4048dbcff56f03bfaf1
- Visualization 5 corresponds to Fig. 4(d) in the main paper (positive-contrast smiley face), together with the more detailed version in Fig. S2(e) of this Supplement. https://opticapublishing.figshare.com/s/bf6a2562b18e1f7891d0

Table S2. Breakdown of which masks were employed for each of the Maxipix ghost projections, in Figs. 3(f) and 4(a-e) from the main paper. Here, the column titles are abbreviated as follows: *F40* – random-fractal mask with 40 μm feature size, *F20* – random-fractal mask with 20 μm feature size, *R40* – binary random mask with 40 μm feature size, *G20* – binarized Gaussian-smoothed-noise mask with 20 μm feature size, *L20* – binarized Lorentzian-smoothed-noise mask with 20 μm feature size, *FRT40* – finite Radon transform based Legendre mask with 40 μm feature size and $p = 127$, N' – number of selected masks.

Target	*F40*	*F20*	*R40*	*G20*	*L20*	*FRT40*	N'
Fig. 3(f)	259	492	-	-	69	-	820
Fig. 4(a)	92	-	-	-	-	-	92
Fig. 4(b)	-	-	-	-	265	-	265
Fig. 4(c)	-	164	140	35	101	50	490
Fig. 4(d)	-	132	135	57	75	64	463
Fig. 4(e)	-	149	-	86	128	25	388

- Visualization 6 corresponds to Fig. 4(e) in the main paper (negative-contrast segment of the ESRF logo), together with the more detailed version in Fig. S2(f) of this Supplement. https://opticapublishing.figshare.com/s/9e8da8b7fc44f36f5938

REFERENCES

1. A. N. Gorban, I. Y. Tyukin, D. V. Prokhorov, and K. I. Sofeikov, "Approximation with random bases: Pro et contra," Inf. Sci. **364–365**, 129–145 (2016).
2. H. H. Barrett and K. J. Myers, *Foundations of Image Science* (John Wiley & Sons, Hoboken NJ, 2004).
3. D. M. Paganin, "Writing arbitrary distributions of radiant exposure by scanning a single illuminated spatially random screen," Phys. Rev. A **100**, 063823 (2019).
4. D. Ceddia and D. M. Paganin, "Ghost projection," Phys. Rev. A **105**, 013512 (2022).
5. D. Ceddia, A. M. Kingston, D. Pelliccia, A. Rack, and D. M. Paganin, "Ghost projection. II. Beam shaping using realistic spatially random masks," Phys. Rev. A **106**, 033512 (2022).
6. J. H. Shapiro, "Computational ghost imaging," Phys. Rev. A **78**, 061802 (2008).
7. J. H. Shapiro and R. W. Boyd, "The physics of ghost imaging," Quantum Inf. Process. **11**, 949–993 (2012).
8. M. J. Padgett and R. W. Boyd, "An introduction to ghost imaging: quantum and classical," Phil. Trans. R. Soc. A **375**, 20160233 (2017).
9. L. Mandel and E. Wolf, *Optical Coherence and Quantum Optics* (Cambridge University Press, Cambridge, 1995).
10. Y. Nakanishi-Ohno, T. Obuchi, M. Okada, and Y. Kabashima, "Sparse approximation based on a random overcomplete basis," J. Stat. Mech. **2016**, 063302 (2016).
11. E. J. Candès and T. Tao, "Near-optimal signal recovery from random projections: Universal encoding strategies?" IEEE Trans. Inf. Theory **52**, 5406–5425 (2006).
12. D. L. Donoho, "Compressed sensing," IEEE Trans. Inf. Theory **52**, 1289–1306 (2006).
13. M. Rani, S. B. Dhok, and R. B. Deshmukh, "A systematic review of compressive sensing: Concepts, implementations and applications," IEEE Access **6**, 4875–4894 (2018).
14. A. M. Kingston, A. Aminzadeh, L. Roberts, D. Pelliccia, I. D. Svalbe, and D. M. Paganin, "Optimizing nonconfigurable, transversely displaced masks for illumination patterns in classical ghost imaging," Phys. Rev. A **107**, 023524 (2023).
15. C. Ponchut, J. M. Rigal, J. Clément, E. Papillon, A. Homs, and S. Petitdemange, "MAXIPIX, a fast readout photon-counting X-ray area detector for synchrotron applications," J. Inst. **6**, C01069 (2011).
16. J. P. Sethna, *Statistical Mechanics: Entropy, Order Parameters and Complexity* (Oxford University Press, Oxford, 2006).
17. W. H. Press, S. A. Teukolsky, W. T. Vetterling, and B. P. Flannery, *Numerical Recipes: The Art of*

Scientific Computing (Cambridge University Press, Cambridge, 2007), 3rd ed.
18. K. Huang, *Statistical Mechanics* (Wiley, New York, USA, 1987), 2nd ed.
19. T. Petersen, M. Ceko, D. Paganin, and I. Svalbe, "A curious invariance property of certain perfect Legendre arrays: Stirring without mixing," in *Discrete Geometry and Mathematical Morphology: Second International Joint Conference, DGMM 2022, Strasbourg, France, October 24–27, 2022, Proceedings,* (Springer, 2022), pp. 330–340.